Hamming distance and the onset of quantum criticality

Tian-Cheng Yi,[1] Richard T. Scalettar,[2,*] and Rubem Mondaini [1,†]

[1]*Beijing Computational Science Research Center, Beijing 100193, China*
[2]*Department of Physics, University of California, Davis, California 95616, USA*

Simulating models for quantum correlated matter unveils the inherent limitations of deterministic classical computations. In particular, in the case of quantum Monte Carlo methods, this is manifested by the emergence of negative weight configurations in the sampling, that is, the sign problem (SP). There have been several recent calculations which exploit the SP to locate underlying critical behavior. Here, utilizing a metric that quantifies phase-space ergodicity in such sampling, the Hamming distance, we suggest a significant advance on these ideas to extract the location of quantum critical points in various fermionic models, in spite of the presence of a severe SP. Combined with other methods, exact diagonalization in our case, it elucidates both the nature of the different phases as well as their location, as we demonstrate explicitly for the honeycomb and triangular Hubbard models, in both their U(1) and SU(2) forms. Our approach exemplifies a possible path allowing the exploration of the phase diagram of a variety of fermionic quantum models hitherto considered to be impractical via quantum Monte Carlo simulations.

I. INTRODUCTION

Extracting unbiased properties of quantum many-body systems exposes the challenge that numerical simulations in classical computers face in exploring quantum matter. Roughly put, one is trapped in a tale of two exponentials. On one side, a constraint arises due to the "exponential wall" associated with the growing dimension of the Hilbert space with the system size. On the other side, in avoiding retrieving exact quantum many-body wave functions and settling instead for a statistical estimation of physical quantities, one ends up facing the sign problem [1], which also leads to an exponential scaling of simulation times. Apart from some special (albeit important) limits, such as the half-filled fermion Hubbard model [2], the latter "wall" appears to be a generic (unavoidable) characteristic of quantum Monte Carlo (QMC) methods for fermionic and frustrated bosonic systems and is conjectured to be NP-hard in a class of spin-glass models [3].

While recent studies have in fact suggested that the average sign of weights in the latter already pinpoints the regimes of strong quantum fluctuations [4–7], here we focus on other statistical properties that also aid in locating quantum phase transitions. In particular, we investigate a specific class of QMC methods for d-dimensional fermionic systems, referred to as auxiliary field QMC [2,8,9], which provides a framework to stochastically average observables by sampling a fictitious field in $d + 1$ dimensions, introduced in a path integral formulation of the partition function. Dubbed the Hubbard-Stratonovich (HS) field [10–13], $s_{i,\tau}$ carries both space and imaginary time labels and decouples the interactions, allowing

an exact integration of the fermionic degrees of freedom (see Appendix A). The statistical properties of $s_{i,\tau}$ are the central object of our analysis.

Recent approaches classified as "machine learning" methods, including convolutional neural networks for pattern recognition [14–16] or clustering methods [17–19], have been applied with the aim of estimating the location of quantum critical points of many-body models using either the HS field or metrics related to it (such as matrix elements of the fermion Green's function) as an input. The fundamental observation of this paper is that the sampled Hamming distance, a simple quantity useful for establishing a separation of two points in the multidimensional phase space of auxiliary field configurations [which we take as discrete; see Fig. 1(a)], already contains information regarding the onset of an ordered phase. Our method certainly *does not* solve the SP, but allows one to extract quantum critical points *in spite* of it.

The Hamming distance is generally defined as a metric for comparing two equal-length data strings, quantifying an elementwise deviation between them. In the case of *binary* strings $x = \pm 1$, it can be written in terms of their inner product

$$\mathcal{H}D_{x,x'} = [1 - \langle x|x'\rangle/\ell]/2, \tag{1}$$

where ℓ is the length of the string and $\langle\cdot|\cdot\rangle$ the standard vector dot product. Identical and opposite (i.e., parity reversed) strings x, x' result in $\mathcal{H}D_{x,x'} = 0$ and $\mathcal{H}D_{x,x'} = 1$, respectively, whereas completely uncorrelated strings are on average $\mathcal{H}D_{x,x'} = 1/2$ apart. In the case of the HS field for local (or intraorbital) interactions, $\ell = N_s L_\tau$, where N_s is the number of orbitals in the real-space lattice and L_τ gives the number of imaginary-time slices in the path integral discretization of inverse temperature $\beta = \Delta\tau L_\tau$.

Nonlocal (or interorbital) interactions, especially nearest-neighbor ones, lead to an HS field that resides on the bonds

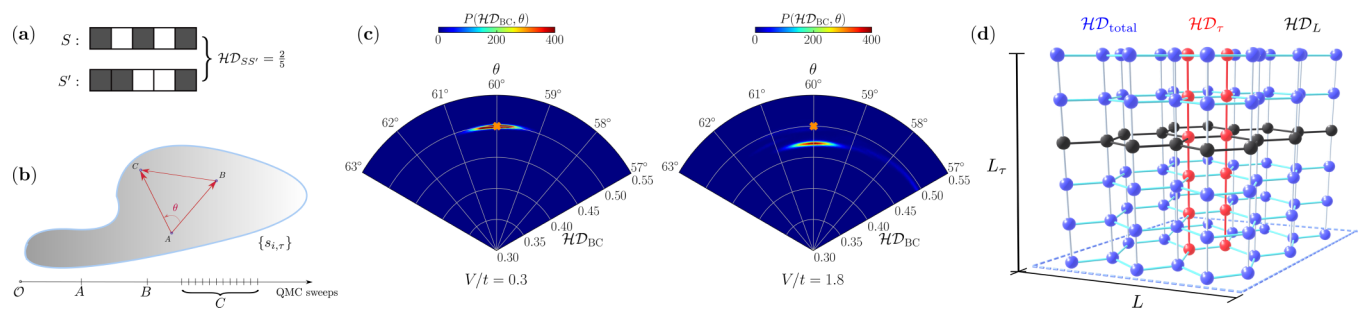*scalettar@physics.ucdavis.edu
†rmondaini@csrc.ac.cn

FIG. 1. Hamming distance and phase space exploration. (a) Representation of the Hamming distance between a pair of binary strings with length 5. (b) Cartoon illustrating the phase space of auxiliary field configurations, accompanied by the protocol used to extract $\mathcal{HD}$ and a *similarity* angle θ in respect to fixed points A and B, selected after two consecutive warmup processes. (c) The corresponding polar probability density of BC Hamming distances for interactions far below (left) and far above (right) the known critical point of the U(1) Hubbard model on the honeycomb lattice, $V_c/t \simeq 1.35$ [20,21]. Cross markers depict the uncorrelated point, $\theta = 60°$ and $\mathcal{HD}_{BC} = 0.5$. (d) Schematic representation of the $3d$ lattice, which arises after the introduction of an auxiliary field $\{S\}$ to decouple the interactions, here on a honeycomb spatial lattice with linear size L and L_τ imaginary-time slices. In the case of intraorbital interactions, the discrete field $\{s_{i,\tau}\}$ lives on the sites (spheres); for interorbital ones, it resides on the bonds connecting sites i and j, $\{s_{ij,\tau}\}$. Different colored spheres and bonds help identify the three types of Hamming distance we compute: Total ($\mathcal{HD}_{total}$), where all fields $\{s_{i\tau}\}$ are considered, $\mathcal{HD}_L$, where we restrict auxiliary-field "strings" to imaginary-time slice $\tau = \beta/2$, and $\mathcal{HD}_\tau$, where the HS field on a single site (or unit cell) across the different L_τ's is monitored. Color code schematically identifies those (see Appendix A for the specific definitions). In (c), the parameters are $L = 12$ and $L_\tau = 240$.

connecting different orbitals [22], whose total number we denote by N_b. Thus the *volume* of the phase space composed by binary strings in these two cases is given by either $2^{N_s L_\tau}$ or $2^{N_b L_\tau}$. Typical importance samplings span a very small region of this vast phase space, but, as we shall see, physical aspects of the model under consideration steer the sampling to correlated configurations within ordered phases, allowing one to quantitatively infer their onset.

This becomes apparent by recalling that the HS field, and in particular correlations between its constituents, serves as a proxy for correlations in real space. As demonstrated by Hirsch for the Hubbard model [12,23], the interorbital fermionic spin correlations $\langle \hat{m}_i(\tau)\hat{m}_j(0)\rangle$ (where $\hat{m}_i \equiv \hat{n}_{i\uparrow} - \hat{n}_{i\downarrow}$ is the local magnetization) are directly proportional to the interspin correlations of the auxiliary bosonic field, $\langle s_{i,\tau} s_{j,0}\rangle$, with the proportionality constant $\alpha = [1 - \exp(-\Delta\tau U)]^{-1}$ and U the strength of the electron-electron interaction.

On an extreme case, when heading towards the atomic limit ($U \to \infty$), for example, the fermionic spin correlations have a one-to-one mapping to the correlations among the "spins" of the HS field (i.e., $\alpha = 1$), provided that the convergence to the continuous of the path integral discretization is slower than the one-site limit is approached [24]. In the case of one fermion per lattice site, the effective Hamiltonian leads to a spin pattern mimicking a Néel state in this regime. As a consequence, field configurations that follow this spin texture have a much larger weight in the sampling, driving it to a vanishingly small region of the phase space [25]. In practice, similar reasoning can be applied to *classical* spin models, although in such cases the spins are to be interpreted as physically relevant quantities; see Appendix B.

To understand how this reasoning translates to regimes far from the classical one, we investigate two models, the U(1) and SU(2) Hubbard models, in two different geometries—honeycomb and triangular lattices. The former serves as a benchmark in which the quantum critical points separating unordered and ordered phases are well established [20,21,26–31]. We then build on that benchmark and show that an

investigation of the model on a triangular lattice allows us to predict the location of quantum critical points which are mostly under debate. These are the cases where known results come from methods that try to conquer the first exponential (the growing size of the Hilbert space), either via bounding the entanglement as in matrix product-states methods in quasi-one-dimensional geometries [32–35] or via exact diagonalization (ED) in small lattices [36–38], including its cluster derivatives [39,40].

II. MODELS

We investigate the spinful,

$$\hat{H} = -t \sum_{\langle ij\rangle\sigma} \hat{c}^\dagger_{i\sigma}\hat{c}_{j\sigma} - \mu \sum_{i\sigma} \hat{n}_{i\sigma} + U \sum_i \hat{n}_{i\uparrow}\hat{n}_{i\downarrow}, \quad (2)$$

and the spinless,

$$\hat{H} = -t \sum_{\langle ij\rangle} \hat{c}^\dagger_i\hat{c}_j - \mu \sum_i \hat{n}_i + V \sum_{\langle ij\rangle} \hat{n}_i\hat{n}_j, \quad (3)$$

Hubbard Hamiltonians, where $\hat{c}_{i\sigma}$ ($\hat{c}_i$) is the pseudospin-σ (spinless) fermion annihilation operator on site i and $\hat{n}_{i\sigma} = \hat{c}^\dagger_{i\sigma}\hat{c}_{i\sigma}$ ($\hat{n}_i = \hat{c}^\dagger_i c_i$) is the corresponding number density operator. Nearest-neighbor hoppings, chemical potential, and repulsive interactions are given by t, μ, and U (V), respectively. The honeycomb and triangular geometries have a total number of sites $N_s = 2L^2$ and $N_s = L^2$; imaginary-time discretization is set at $t\Delta\tau = 0.1$.

The models on the (bipartite) honeycomb lattice are investigated at $\mu = U/2$ and $3V$, which yields "half filling" in the SU(2) and U(1) versions of the Hamiltonian, respectively. For the triangular lattice, on the other hand, the chemical potential is systematically tuned in the $[T \equiv 1/\beta, U(V), N_s]$ set of parameters to yield one fermion per site in the spinful formulation and one fermion per elemental triangle in its spinless version. The latter is chosen such as to render a sharp quantum phase transition to a 1/3-filled charge density wave (CDW) state that emerges as the interactions V are increased.

III. U(1) HONEYCOMB HUBBARD MODEL

The computation of the Hamming distance between configurations of the phase space is equivalent to a projection $2^{N_b L_\tau} \to 1$ on the number of degrees of freedom. This scaling-down process is prone to miss significant features of the sampled fields and eventually not fully characterize what is driving the sampling to become correlated. An improvement in this approach is to investigate projections to *two* degrees of freedom instead. For that we take two points in the generated Markov chain, each after a significant warmup in the QMC sweeps. Thus proceeding with the usual importance sampling, while storing the distances between such points in the phase space, as illustrated in Fig. 1(b), one can define a similarity metric between configurations, i.e., an angle θ in phase space encompassed by the Hamming distance between two points in respect to a third one, i.e.,

$$\theta = \cos^{-1}\left(\frac{\mathcal{H}D_{AB}^2 + \mathcal{H}D_{AC}^2 - \mathcal{H}D_{BC}^2}{2\mathcal{H}D_{AB}\mathcal{H}D_{AC}}\right). \quad (4)$$

Uncorrelated configurations form equilateral triangles in $\{s_{ij,\tau}\}$ (i.e., $\theta = 60°$) and deviations from this signal a certain degree of correlations in the sampling.

Figure 1(c) tests this for the case of the U(1) honeycomb Hubbard model, at interactions far above and far below the known critical point $V_c/t \simeq 1.35$ [20,21], separating a Dirac semimetal from a charge density-wave (CDW) Mott insulator. While the majority of the angles still denote uncorrelation at either side of the transition, the typical Hamming distance significantly departs from $1/2$ for $V > V_c$. For that reason, we hereafter focus primarily on $\overline{\mathcal{H}D} \equiv \overline{\mathcal{H}D_{BC}}$, the average Hamming distance, aiming at observing a signature of the known QCP location for this model. In addition, we also compute the average Hamming distance selecting fields within a fixed real space unit cell across L_τ ($\mathcal{H}D_\tau$) or within fixed imaginary-time "layers" over real space ($\mathcal{H}D_L$)—see Fig. 1(d) for a schematic representation [41]. The goal is to understand if the appearance of structure in the manifold of typical field configurations visited in the course of the sampling has a preferential dimension.

Figure 2(a) exhibits these different quantities for a lattice with linear size $L = 12$ at $T/t = 1/24$. Remarkably, a sharp departure from $\mathcal{H}D = 1/2$ is obtained around V_c/t, a feature largely system size independent [Fig. 2(c)] when approaching the $T \to 0$ limit [Fig. 2(b)]. Furthermore, except for minor statistical fluctuations, no significant deviations are found between the different types of averaged Hamming distances in this model, as the onset of structure in the data set simultaneously occurs in all three.

IV. SU(2) HONEYCOMB HUBBARD MODEL

In analogy to the spinless version, its spinful generalization features the onset of a Mott insulator at sufficiently large (local) interactions, supplanting a Dirac semimetal phase. The insulating phase, however, exhibits a spin-density wave (SDW), i.e., antiferromagnetic order that is triggered at $U_c/t \simeq 3.8$ [28–31]. Figure 3 displays the equivalent of Fig. 2 for this Hamiltonian. Apart from larger fluctuations (even more pronounced for $\mathcal{H}D_\tau$; see Appendix D), and a less
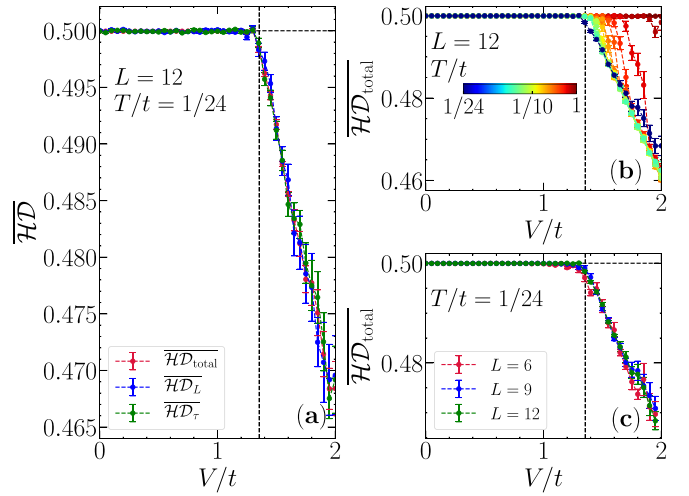

FIG. 2. Hamming distance for the spinless honeycomb Hubbard model. (a) The three types of Hamming distance (see text), $\mathcal{H}D_{\text{total}}$, $\mathcal{H}D_L$, and $\mathcal{H}D_\tau$ vs V/t, as marked. Vertical dashed line displays the QCP obtained in Ref. [21], $V_c/t = 1.355 \pm 0.001$. (b) Temperature dependence of $\mathcal{H}D_{\text{total}}$ on the interactions with $L = 12$. (c) Finite-size comparison of the total Hamming distance vs V at $T/t = 1/24$. For this case with a discrete symmetry breaking, the thermal transition can also be seen at values of the interactions that $\mathcal{H}D$ departs from $1/2$ at finite temperatures; see Appendix C. Error bars depict the standard error of the mean (s.e.m.) over 48 independent Markov chains.

marked deviation from the uncorrelated sampling regime, the Hamming distance similarly tracks the onset of the ordered phase.
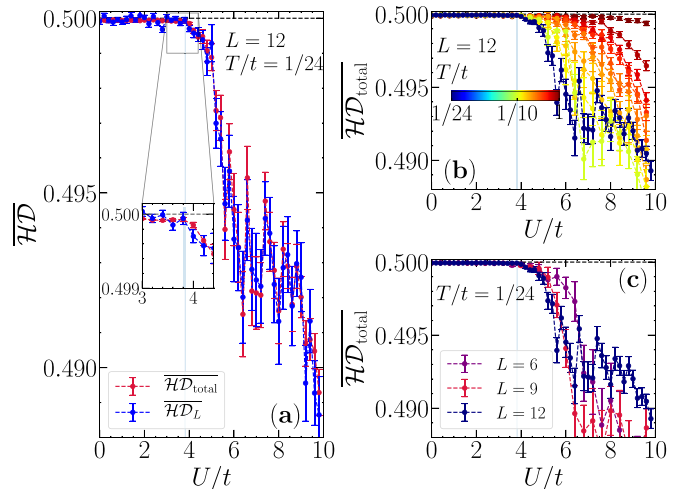

FIG. 3. Hamming distance for the spinful honeycomb Hubbard model. (a) Total and the $\tau = \beta/2$ Hamming distances when the local interactions U are swept for a honeycomb lattice with $N_s = 288$ sites at $T/t = 1/24$. Inset displays a zoom-in on the region close to the know QCP for this model. Panels (b) and (c) give the temperature and system-size dependence, respectively, with increasing U for $\mathcal{H}D_{\text{total}}$. Vertical shaded region depicts a confidence region of the QCP based on recent results in the literature [28–31]. Error bars display the s.e.m. for 48 independent realizations.

Strong fluctuations on this spinful case can be interpreted by means of the larger cardinality of local degrees of freedom (four instead of two for the spinless Hamiltonian) and that the same bosonic field $\{s_{i,\tau}\}$ couples to *both* fermionic flavors. Moreover, as the Mermin-Wagner theorem states that the formation of long-range magnetic order on a system with continuous symmetry at $T \neq 0$ is precluded for $d \leqslant 2$ [42,43], any finite-temperature departure of $\mathcal{H}D = 1/2$ is understood in terms of the minimum temperature at which the quickly decaying correlations reach typical correlation lengths comparable to the system size. This is not the case for its U(1) counterpart with a discrete symmetry breaking, in which a finite-T transition signified by the loci where $\mathcal{H}D < 1/2$ quantitatively matches known results for this model (see Appendix C).

V. U(1) TRIANGULAR HUBBARD MODEL

Building on those results, we investigate a model in which there is no known solution to circumvent the sign problem, i.e., the geometrically frustrated triangular lattice Hubbard model. Starting from its spinless formulation, we notice that in between commensurate densities, as 1/3 and 2/3 fillings, a *pinball liquid* phase arises, in which CDW order coexists with metallic behavior [36,38]; this intermediate phase corresponds to a supersolid in the case of hardcore bosons [44]. With the goal of exploring a well marked QCP, we study the case of one fermion for every three lattice sites. As previously stated at the end of Sec. II, this 1/3-CDW phase is inferred from the connection to the atomic limit ($V/t \to \infty$), wherein such a charge configuration minimizes the total energy. In the presence of quantum fluctuations, one then expects that sufficiently large interactions trigger an ordered regime.

Even though the specific location of the critical interaction strength that leads to a form of Wigner solid is currently not known, the average Hamming distance analysis when sweeping V shows a well marked transition at $V_c/t = 2.85(2)$ [Fig. 4(a)]. ED results (see Appendix F) in smaller lattices ($L = 6$) can capture a continuous transition to the ordered regime at $V/t \simeq 2.7$ instead, highlighting the importance of finite-size effects in determining the QCP location. Temperature and lattice size dependence in these results are displayed in Figs. 4(b) and 4(c), respectively. The former shows a subtle nonmonotonic behavior of $\overline{\mathcal{H}D}$ within the ordered phase when T is decreased, whose origin will be explored in detail for the spinful version in what follows. Whether the average Hamming distance is sufficiently sensitive to be used in the identification of the regime of coexistence of CDW and metallicity (pinball liquid), thought to occur beyond commensurate densities, will be left for future studies.

VI. SU(2) TRIANGULAR HUBBARD MODEL

The ingredient that allows both insulating and antiferromagnetic transitions to concomitantly occur on the SU(2) Hubbard model with growing interactions, i.e., that the cluster structure is bipartite, is no longer present in a triangular lattice. As a result, early studies within approaches that try to conquer the first exponential "wall" managed to demonstrate the existence of an intermediate nonmagnetic insulating (NMI)
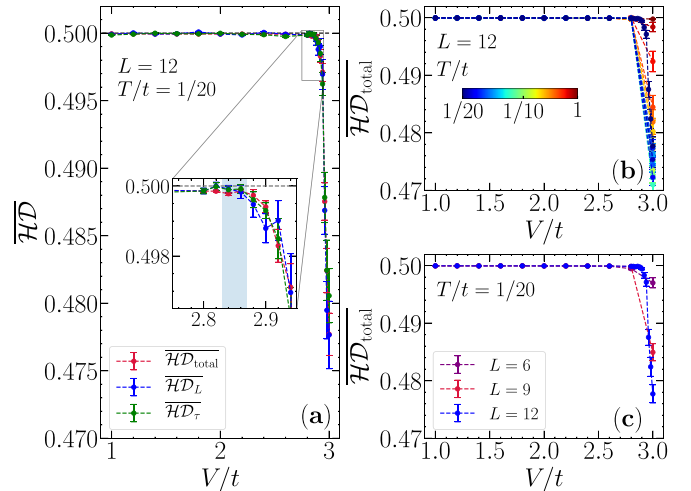

FIG. 4. Hamming distance for the spinless triangular Hubbard model. (a) The different averaged Hamming distances with increasing repulsive nearest-neighbor interactions V. The inset displays a zoom-in of the location where $\mathcal{H}D$ departs from 1/2, accompanied by a shaded region marking a confidence interval of the ordered phase onset for an $L = 12$ lattice at $T/t = 1/20$. Panel (b) shows the total Hamming distance with decreasing temperature, while (c) displays its finite-size effects at $T/t = 1/20$. ED results give a transition at $V/t \simeq 2.7$ on an $L = 6$ lattice (Appendix F), which can be approached via a $\Delta\tau \to 0$ extrapolation in a similar lattice size (Appendix E).

phase, separating the metallic regime at small interactions and the magnetically ordered phase at large values of U/t [39,40,45,45]. In the latter, the low-energy effective model maps to the antiferromagnetic Heisenberg model, in which a 120° Néel ordered phase has been shown to be stabilized to compose with the geometric frustration [46,47].

The nature of the intermediate NMI phase has been investigated within density matrix renormalization group (DMRG) methods [32–35] and recent results have pointed to the possibility that this phase realizes a gapped chiral spin liquid [33,35], at least in some of the lattice structures amenable to computations. Importantly, molecular crystals of the κ-ET family are known to be close experimental realizations of such triangular lattice Hubbard models [48,49] and, in particular, compounds such as κ-(ET)$_2$Cu$_2$(CN)$_3$ have a quasi-isotropic hopping structure in the lattice [50], which does not exhibit any magnetic ordering down to 32 mK, indicative that it may indeed host a spin liquid ground state.

Despite the strong motivation provided by these exciting results, progress has been significantly impeded because the corresponding model has a drastic sign problem (see Appendix G) and QMC calculations have large error bars stemming from the second exponential wall we described in the Introduction. Nevertheless, as Fig. 5 shows, although extremely challenging to extract physical quantities, the onset of the ordered phase can be very successfully observed via the average Hamming distance. The deviation from the uncorrelated case ($\overline{\mathcal{H}D} = 1/2$) is seen to be reasonably well aligned to the most recent predictions on this model [33,35]. Finite-size effects are shown to be small in Fig. 5(c), while, similar to the spinless fermion counterpart, the average Hamming distance
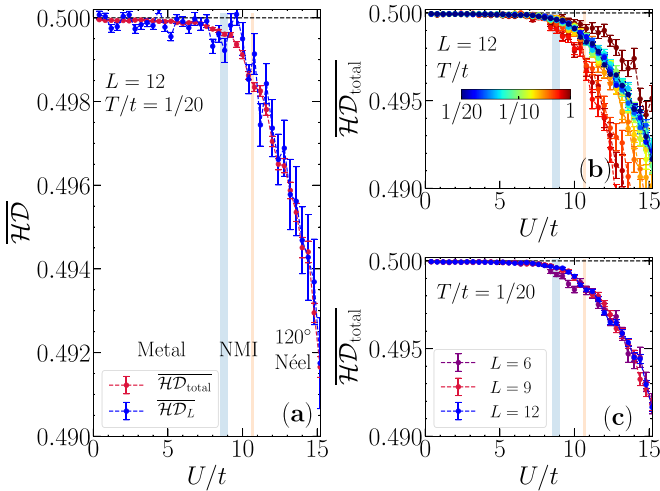
FIG. 5. Hamming distance for the spinful triangular Hubbard model. Similar to Fig. 2, but for the SU(2) Hubbard model on the triangular lattice. (a) Total and $\tau = \beta/2$ average Hamming distances, (b) temperature dependence of the Hamming distance for a fixed lattice size ($N_s = 144$), and (c) the finite-size effects obtained at $T/t = 0.05$. Shaded vertical regions in all panels display the combined results from Refs. [33,35] obtained for width-4 cylinders with finite or infinite lengths; they mark transitions at $U_{c1}/t = 8.5$–9 and $U_{c2}/t = 10.6$–10.75.
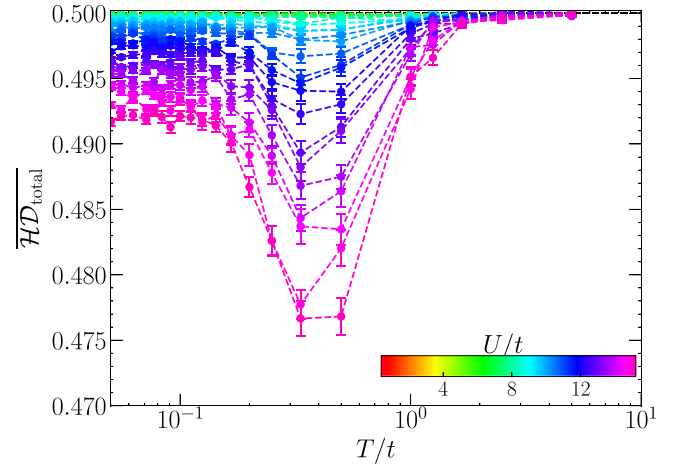

FIG. 6. Order-by-disorder effects in the Hamming distance. Hamming distance for the spinful triangular Hubbard model vs T for various interaction strengths U in an $L = 12$ lattice. The decrease in the Hamming distance upon heating, that is, the increase of localization in the phase space, parallels a similar effect observed for a physical quantity, the double occupancy, a proxy for electronic localization [34,40], whose minima occur at compatible temperatures.

departs from $1/2$ in a nonmonotonic fashion with decreasing temperatures, as seen in Fig. 5(b). An explanation for such seemingly unexpected behavior is provided in what follows.

Although a clear-cut location of the QCP is likely only obtained in the $\Delta\tau \to 0$ limit [see such analysis for the U(1) honeycomb Hubbard model in Appendix E], there is manifest evidence that the Hamming distance does capture physically relevant information. An argument in this direction can be put forward by early observations that point out that the interplay of geometric frustration and interactions may lead to ground states with large thermal entropies S when entering the ordered regime. In turn, the positive variation of S with interactions, at fixed T, can be related to the decrease of the double occupancy $D = (1/N_s) \sum_i \langle \hat{n}_{i\uparrow} \hat{n}_{i\downarrow} \rangle$ with temperature (at fixed U) via a Maxwell relation [34,40,51]

$$\left. \frac{\partial S}{\partial U} \right|_T = -\left. \frac{\partial D}{\partial T} \right|_U. \tag{5}$$

As a consequence, the double occupancy at sufficiently small T's decreases with temperature, an effect at odds with what one would expect from the connection of D with localization (in the $U/t \to \infty$ limit, $D \to 0$). This increase of electron localization upon heating, referred to as order by disorder, can be similarly seen in Fig. 6, by means of localization in phase space described by a reduced Hamming distance. A further confirmation of the unexpected $D \leftrightarrow \mathcal{HD}$ connection can be made by noticing that the minima of both quantities are seen at similar temperatures $T/t \approx 0.5$ [34].

VII. DISCUSSION AND OUTLOOK

A common thread in the study of quantum correlated matter is that if a given model is plagued by the sign problem

when utilizing a QMC method, and the aim is to extract properties close to $T = 0$, there is not much one can do and the application of other numerical methods would consist of a better use of resources. This reasoning is based on the computationally expensive "wall" that prevents a statistically convergent estimation of physical quantities within reasonable time. What we have shown here is that other statistical metrics host information about the onset of ordered phases, at least on the limited class of problems we have studied. This is clearly seen via the average distance in phase space spanned on the course of the importance sampling, but other complementing metrics, such as the intrinsic dimension or the variance of nearest-neighbor configurations [17,18] might reveal even finer details, in particular finite-size scaling exhibiting the universality class of the transitions by means of the extraction of critical exponents; statistical fluctuations of the average Hamming distance elude such analysis in our case. That is, the Hamming distance is seemingly a less sensitive quantity in this regard.

Additionally, it is important to emphasize that while our results quantitatively point out regimes in which the connection exists, i.e., quantum critical point location being identified by the onset of a reduced Hamming distance, by no means does this solve the sign problem. One could potentially study even a wider class of models plagued by the occurrence of negative weights in the sampling in which a statistical analysis of the auxiliary fields may not point out the occurrence of a quantum ordered regime. Here, in the cases in which the sign problem is most dramatic, the triangular lattice versions of the models, either the comparison to exact diagonalization in small systems (Appendix F) and existing results using large scale calculations in cylinders [32–35] indicate that such connection holds, but again the issue of the generality of these results remains.

Models featuring deconfined quantum critical points (DQCPs) [52], that is, separating two symmetry-incompatible ordered phases [53], are likely challenging to investigate using our approach. Nonetheless, a possible approach is to compare the average Hamming distance between configurations using slightly different Hamiltonian parameters. A likely outcome is that, at sufficiently low temperatures, typical configurations sampled in parallel are on average far apart if the parameters are chosen such that they belong to different ordered phases. By systematically reducing the parameter's deviation, the point at which the $\mathcal{H}D$ decreases potentially signals the DQCP location. We leave this line of inquiry for future studies.

Lastly, it remains to be seen if the highly nonlocal action for the resulting HS fields that arises after the fermionic integration may define a spin glass at sufficiently low temperatures and its eventual connection to negative weight configurations. The Hamming distance, intimately related to the spin-glass order parameter [54], has been used to quantify the ultrametricity of the phase space in classical models [55], a characteristic feature of glassy behavior [56].

APPENDIX A: METHODS

Numerical calculations employ the Blanckenbecler-Scalapino-Sugar (BSS) algorithm [2,8] for QMC calculations: The partition is written as a path integral, in which a sequence of Trotter decomposition, HS transformation, and integration of the resulting fermionic bilinear forms allows one to express it as a sum over auxiliary field configurations of determinants of fermionic matrices on a single-particle basis. The sign problem thus arises as the determinants are not guaranteed to be positive definite for arbitrary configurations of the fields. We apply the standard spin decomposition in the HS transformation for the SU(2) models [12],

$$e^{-\Delta\tau U(\hat{n}_{i\uparrow}-\frac{1}{2})(\hat{n}_{i\downarrow}-\frac{1}{2})} = \frac{1}{2}e^{-U\Delta\tau/4}\sum_{s_i=\pm 1}e^{\lambda s_i(\hat{n}_{i\uparrow}-\hat{n}_{i\downarrow})},$$

or its corresponding on the U(1) Hamiltonians [22],

$$e^{-\Delta\tau V(\hat{n}_i-\frac{1}{2})(\hat{n}_j-\frac{1}{2})} = \frac{1}{2}e^{-V\Delta\tau/4}\sum_{s_{ij}=\pm 1}e^{\lambda s_{ij}(\hat{n}_i-\hat{n}_j)},$$

where $\cosh\lambda = e^{U\Delta\tau/2}$ and $\cosh\lambda = e^{V\Delta\tau/2}$, respectively. Note that the auxiliary fields that decouple the interactions have a double index in the latter and reside on the bonds connecting orbitals i and j. The total number of bonds and corresponding number of auxiliary field configurations in a single imaginary-time slice is $N_b = 3L^2$ in either the honeycomb or triangular lattices. We do not make use of the Majorana representation [21]; thus our simulations are affected by the sign

problem in the U(1) honeycomb Hubbard model, which is irrelevant for our results, and highlight the predictive power of statistical properties of the importance sampling. Simulations are carried out employing typically thousands of QMC sweeps with independently seeded Markov chains ranging from 20 to 48, with Hamming distances with respect to a fixed configuration stored at the end of the warmup process extracted after a full sweep in the space-imaginary-time lattice. For example, for the data presented in Fig. 1, we performed two consecutive 1000 warmup sweeps, storing the corresponding Hubbard-Stratonovich configurations at the end of each warmup, and subsequently computed the Hamming distance to those configurations along 8000 measurement sweeps, using 48 independent realizations. In Appendix F, we further employ ED for the triangular Hubbard model in small clusters, featuring 36 (18) sites in its spinless (spinful) formulation.

Definitions. The various Hamming distances we compute in the manuscript can be written in terms of the inner products as explained in the Introduction or equivalently by means of the L_1 norm,

$$\mathcal{H}D = \frac{1}{2\mathcal{V}}\sum_{i,\tau}\left|s_{i,\tau} - s_{i,\tau}^{\mathrm{ref}}\right|, \tag{A1}$$

where $\{s_{i,\tau}^{\mathrm{ref}}\}$ represents a reference configuration (the one obtained after the warmup sweeps) and the $\mathcal{V}$ denotes the number of elements in the corresponding Hubbard-Stratonovich field. For example, in the case of the SU(2) Hubbard models we study, $\mathcal{V} = \ell = N_s L_\tau$ and the summation is over the whole space-imaginary-time lattice for the "total" Hamming distance, $\mathcal{H}D_{\mathrm{total}}$. $\mathcal{H}D_L$, which takes a single layer at $\tau = \beta/2$, has then $\mathcal{V} = N_s$ and summation in Eq. (A1) is constrained to that imaginary-time slice across the real-space lattice. In turn, $\mathcal{H}D_\tau$, the Hamming distance across imaginary time, takes $\mathcal{V} = 2L_\tau$ for the SU(2) honeycomb Hubbard model and $\mathcal{V} = L_\tau$ in its triangular lattice counterpart; the summation over i in this case is constrained to the central unit cell of the real-space lattice.

Similar definitions hold, for the U(1) Hubbard model, where now the fields $\{s_{ij,\tau}\}$ are on the bonds connecting interacting orbitals i and j,

$$\mathcal{H}D = \frac{1}{2\mathcal{V}}\sum_{\langle ij\rangle,\tau}\left|s_{ij,\tau} - s_{ij,\tau}^{\mathrm{ref}}\right|. \tag{A2}$$

$\mathcal{H}D_{\mathrm{total}}$ takes an unconstrained summation in Eq. (A2), where $\mathcal{V} = 3L^2 L_\tau$ in either honeycomb or triangular lattices. $\mathcal{H}D_L$ constrains the summation within $\tau = \beta/2$; thus $\mathcal{V} = 3L^2$ for both geometries, whereas in $\mathcal{H}D_\tau$, $\mathcal{V} = 3L_\tau$, with bond fields departing from the real-space central site (one site of the central unit cell) across imaginary time for the triangular (honeycomb) lattice.

APPENDIX B: CLASSICAL VS QUANTUM MODELS

To verify that the Hamming distance can be indeed used as a proxy to locate phase transitions either in classical or quantum models, we contrast the results for the U(1) honeycomb Hubbard model, originally presented in the main text, with the ones from the classical Ising model on a square lattice (Fig. 7). The energetics in the latter is given by $E = -J\sum_{\langle i,j\rangle}S_iS_j$,
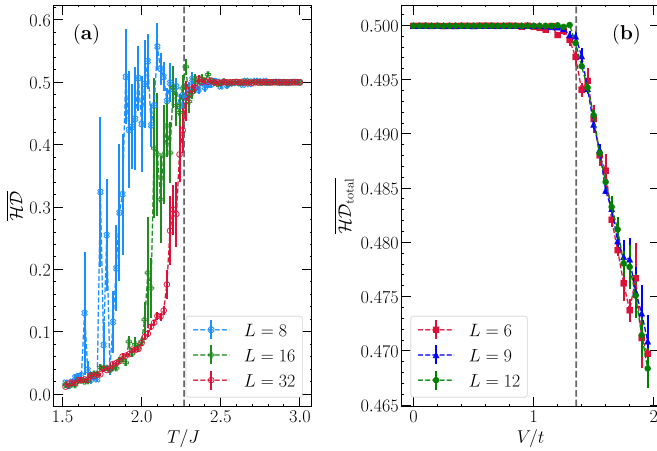
FIG. 7. (a) Average Hamming distance over eight independently seeded Markov chains for the two-dimensional classical Ising model. The distances are computed at the end of a full sweep (N_{sweeps} = 10 000) in respect to a fixed configuration, selected after 1000 warmup sweeps at each temperature T, in a cooling process from the largest temperature. The critical point at $T/J \approx 2.269$ is marked by the vertical dashed line. Here, to parallel the scheme in its quantum counterpart, we use a single-flip update (Metropolis) in opposition to cluster update schemes. (b) Average total Hamming distance of the U(1) honeycomb Hubbard model [similar to Fig. 2(c)]. The vertical dashed line gives the location of the QCP obtained in Refs. [20,21].

where $S_i = \pm 1$ are classical spins. As the linear lattice size L is increased, the drop of the average Hamming distance from its uncorrelated value $\overline{\mathcal{HD}} = 0.5$ systematically approaches the known critical temperature $T_c = 2/\ln(1 + \sqrt{2})$, much in line with what occurs on the *quantum* U(1) honeycomb Hubbard model. The difference here is that although in the classical Ising model the spins are physical, in the quantum model they are auxiliary variables. In both, however, they are sampled on and single-flip updates are performed. While in the classical case there are more sensitive quantities to identify the transition location (e.g., magnetic susceptibilities or Binder cumulants), this analysis highlights the ability of using metrics related to the fields, other than physical quantities, to locate phase transitions.

APPENDIX C: FINITE-TEMPERATURE TRANSITIONS

The U(1) Hubbard model displays a finite-temperature transition to an ordered phase, which has been classified on the honeycomb lattice by means of the continuous-time interaction expansion method [57] or in a hybrid SSE/determinantal approach [58], both of which result in sign-problem free simulations. Here we argue that the metric of phase space exploration we introduced in the main text, the average Hamming distance, similarly captures the thermal transition in the original BSS type algorithm for this model [22]. Figure 8 displays the "phase diagram" of this quantity in the temperature–interactions plane, overlaying it with the results extracted from Ref. [57]. Agreement between these results and the (T, V) parameters at which $\overline{\mathcal{HD}}$ deviates from $1/2$ is reasonably good, presenting an even closer matching when increasing the system size.
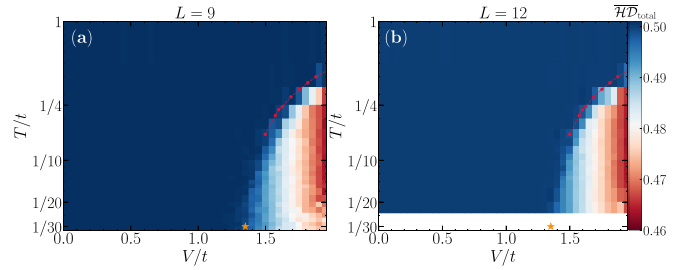

FIG. 8. Thermal transitions via the Hamming distance. Contour plot of the average Hamming distance in the temperature–interactions plane for the t-V Hubbard model on the honeycomb lattice, with linear size $L = 9$ (left) and $L = 12$ (right). Markers are extracted from the results of Ref. [57] and the star at the lowest temperature describes the known QCP location [20,21].

APPENDIX D: LARGE STATISTICAL FLUCTUATIONS IN $\mathcal{HD}_\tau$

As described in the main text, statistical fluctuations in the average Hamming distance within a site (or unit cell) across different imaginary time slices, $\mathcal{HD}_\tau$, are sensibly large, as seen in Fig. 9 for the two SU(2) models we investigate. There are two reasons that can explain such behavior. The first is that the HS field is a massless bosonic field that mediates instantaneous interactions between the fermions traversing the real-space imaginary-time lattice; a consequence of being massless is that wild fluctuations occur in imaginary time (even if the field were to be made continuous [9]). A direct contrast is the case of the Holstein model, where massive phonons play the role that mediate the electronic interactions. In this case, their mass controls the "velocity" of the phonon field in the action, taming the large oscillations in imaginary time. In the absence of such kinetic energy term in the action for the Hubbard model, the field configurations in consecutive imaginary-time slices are not directly coupled. Second, spin orientation patterns for the fermions in approaching the atomic limit are more easily seen through equal-time correlations. Consequently, selecting one unit cell or site to monitor the auxiliary-field configurations does not render a
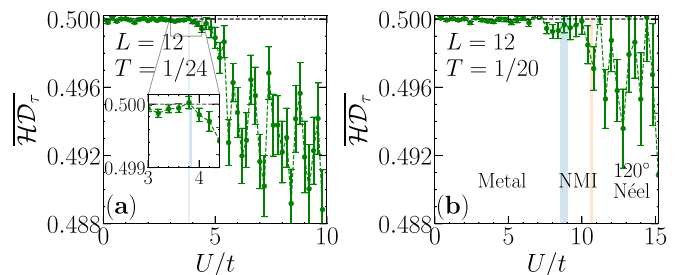

FIG. 9. Fluctuations of the Hamming distance across imaginary time. (a) Average Hamming distance $\overline{\mathcal{HD}_\tau}$ in the spinful honeycomb Hubbard model while sweeping the interactions and (b) the same but for the spinful triangular Hubbard model. Although fluctuations are much larger than the other metrics we investigate, it qualitatively captures the onset of the ordered phase. In both cases the linear lattice size is $L = 12$; the inverse temperature is set at $\beta t = 24$ and 20, respectively.

well defined string that uniquely captures such patterns owing to quantum fluctuations which inherently occur.

APPENDIX E: APPROACHING A CONTINUOUS IMAGINARY TIME

Apart from statistical uncertainties, which are always controllable by the sampling extent, certain QMC simulations (auxiliary-field versions, in particular) are subjected to a single approximation that stems from the Trotter decomposition employed when splitting the exponential operators in the partition function. For the Hubbard model, for example, the simplest decomposition leads to an error $O[tU(\Delta\tau)^2]$. Nonetheless, this approximation can be made controllable by taking the limit $\Delta\tau \to 0$ (at the expense of increasing the number of imaginary-time slices at a fixed temperature) such that it becomes indistinguishable from the statistical fluctuations.

Here in the case of the statistics of the sampling, namely the average Hamming distance, there is another complication that was exposed in the main text when describing the connection between fermionic correlations and correlations between the auxiliary field components. This can be seen via the relation connecting bosonic field correlations and the fermionic ones [12,23]:

$$\langle[\hat{n}_{i\uparrow}(\tau) - \hat{n}_{i\downarrow}(\tau)][\hat{n}_{j\uparrow}(0) - \hat{n}_{j\downarrow}(0)]\rangle = \frac{1}{1 - e^{-\Delta\tau U}}\langle s_{i,\tau}s_{j,0}\rangle,$$
$$(E1)$$

with the exception $i = j$, $\tau = 0$. As we argued there, for the proportionality constant to approach 1 in the atomic limit, it is necessary that the imaginary-time discretization go to zero slower than that. As a result, a relevant analysis is to understand the effect of the imaginary-time discretization on the average Hamming distance. We do so for the U(1) honeycomb Hubbard model, where a crisp connection of the correlated sampling to the onset of the ordered phase was drawn. We notice that in this case of a spinless Hamiltonian, a similar relation as Eq. (E1) can be derived, involving the correlation of density operators $(\hat{n}_i - \hat{n}_j)$ and the corresponding decoupling field $s_{ij,\tau}$ at that bond.

For that end, Fig. 10 shows the average total Hamming distance with decreasing $\Delta\tau$, at a low fixed temperature $T/t = 1/16$ on an $L = 9$ lattice. An asymptotic approach to the known critical point is obtained in the limit $\Delta\tau \to 0$ and values of $\Delta\tau = 0.1$ are sufficiently close to describing the onset of the ordered phase. Similarly, the results for the triangular lattice version are also shown in Fig. 10, bottom, with $T/t = 1/20$ and $L = 6$. This lattice size is amenable to exact numerical computations and the location of the quantum phase transition can be reliably extracted. As for the honeycomb lattice, the departure from $\mathcal{H}D = 1/2$ with decreasing $\Delta\tau$ systematically approaches the exact results.

APPENDIX F: EXACT DIAGONALIZATION RESULTS

Despite being a useful tool to infer the onset of ordered phases, the average Hamming distance does not aid in understanding the precise nature of those phases. The honeycomb lattice models we study are well understood, but the triangular lattice versions are slightly less explored. For that reason,
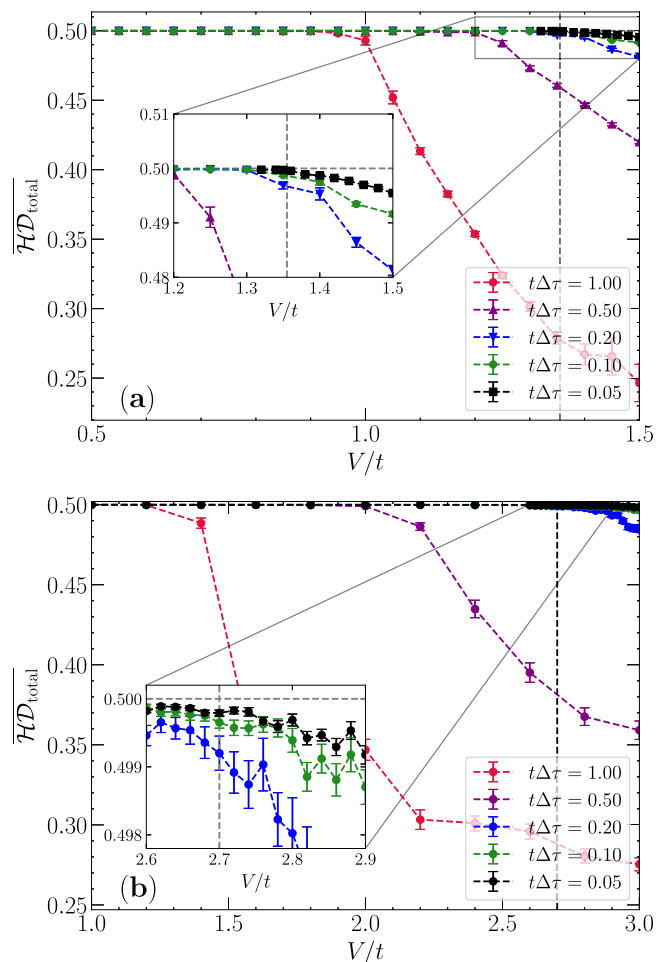

FIG. 10. Hamming distance dependence on the imaginary-time discretization. (a) Total Hamming distance $\overline{\mathcal{H}D_{\text{total}}}$ in the spinless honeycomb Hubbard model, with a range of imaginary-time discretizations $\Delta\tau$ as marked. Vertical dashed lines give the known critical interaction $V_c = 1.355t$ [20,21] related to the onset of the ordered phase. The inset gives a zoom-in depicting the asymptotic approach to the transition. The linear lattice size is $L = 9$ and the temperature is fixed at $T/t = 1/16$. (b) The same for the spinless triangular Hubbard model, but in an $L = 6$ lattice where the ED results for the quantum critical point location, marked by the vertical dashed line, are extracted by us (see Appendix F); here $T/t = 1/20$.

we make use of exact diagonalization (ED) to corroborate some of these phase transitions and ensuing ordered phases. Constrained by the first exponential wall, we are limited to calculations on small cluster sizes, which we set at 6×6 and 6×3 in the spinless and spinful Hamiltonians, respectively.

We start with the U(1) case, with filling 1/3 (12 fermions in 36 orbitals), as shown in Fig. 11. When sweeping the interactions V we observe a first order phase transition at around $V/t \simeq 1.7$, where the ground state changes from the pseudo-momentum $\vec{q} = (0, 2\pi/3)$ sector to $\vec{q} = (0, 0)$. This leads to discontinuities in several observables, including the average nearest-neighbor density correlations $\langle \hat{n}_i \hat{n}_j \rangle_{\langle ij \rangle}$ [Fig. 11(a)]. We believe that such a transition is cluster dependent. More importantly, there is a clear signal in physical quantities of an actual continuous phase transition at larger interactions,
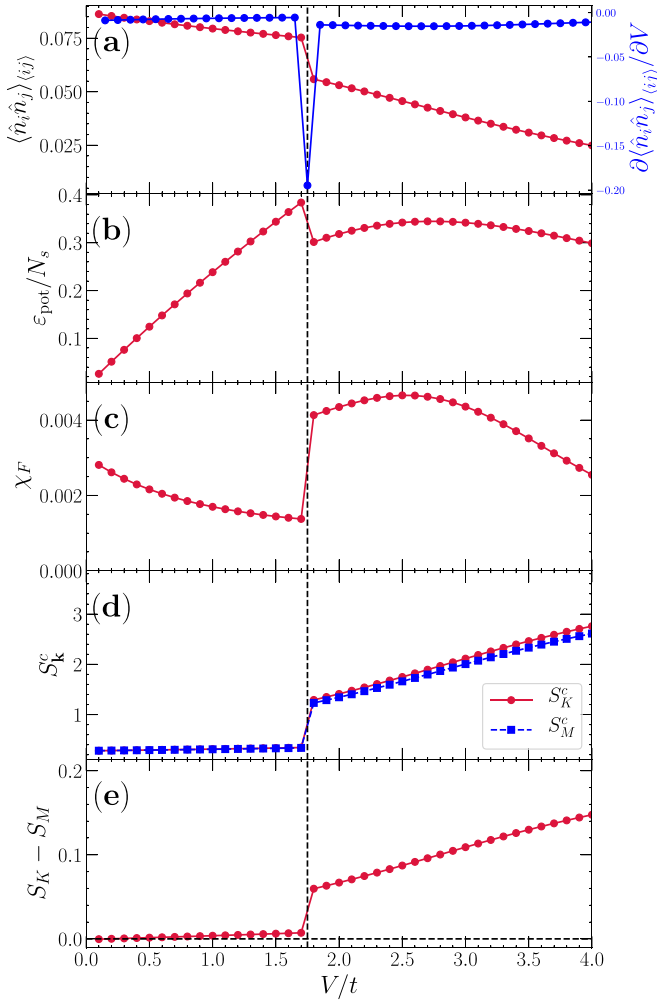
FIG. 11. ED results for the spinless triangular Hubbard model on a 6×6 lattice. (a) Average nearest-neighbor correlation function (left y axis) and its corresponding derivative (right y axis). (b) The vertical dashed lines across all panels mark the location of the first order phase transition observed for this cluster size and where the momentum sector ground state resides changes with V.

likely associated to the onset of the 1/3-CDW phase. A first indication is seen by means of the potential energy $\varepsilon_{\text{pot}} = V \sum_{\langle i,j \rangle} \langle \hat{n}_i \hat{n}_j \rangle$, which displays a peak at around $V/t \simeq 2.7$ [Fig. 11(b)]; past this point one expects that quantum fluctuations are necessarily reduced in heading towards the atomic limit and ε_{pot} decreases. Similar information about the transition can be inferred by the fidelity susceptibility [59],

$$\chi_F = \frac{2}{N_s} \frac{1 - |\langle \Psi_0(V) | \Psi_0(V + dV) \rangle|}{dV^2}, \qquad \text{(F1)}$$

where $|\Psi_0(V)\rangle$ is the ground state with interaction magnitudes V and $dV = 10^{-3}t$ is a small parameter deviation. Extensive peaks (with the system size) signify locations of QCP for continuous transitions, whereas discontinuities are seen within first-order ones. For our specific case of a 36-sites lattice, we observe a peak at around $V/t \simeq 2.5$ [Fig. 11(c)].
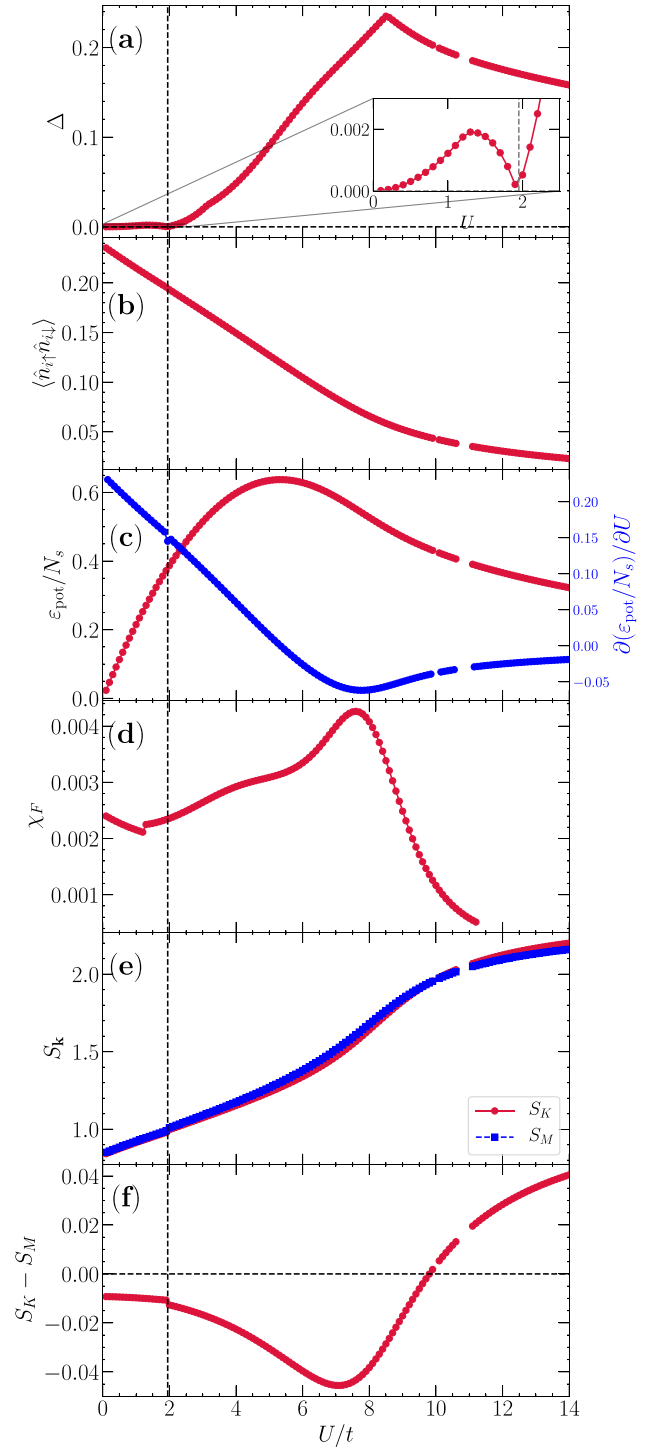

FIG. 12. ED results for the spinful triangular Hubbard model on a 6×3 cluster. (a) The many-body gap $\Delta = |E_{(0,0)}^{\text{GS}} - E_{(0,4\pi/3)}^{\text{GS}}|$ comparing the lowest energy states at different momentum sectors. The inset magnifies the results showing a first order phase transition occurring at $U/t \simeq 1.9$. (b) The double occupancy at the ground state and (c) the potential energy vs U/t. The inflection point in the latter likely gives the metal-insulating transition point ($U/t \simeq 7.6$) which coincides with the peak of the fidelity susceptibility shown in (d). (e) The spin structure factor at different high symmetry points and (f) the difference of the results for K and M points in the Brillouin zone. They point to enhanced stripy antiferromagnetic correlations which give way to a Néel 120° order at $U/t \simeq 10$ (see text).
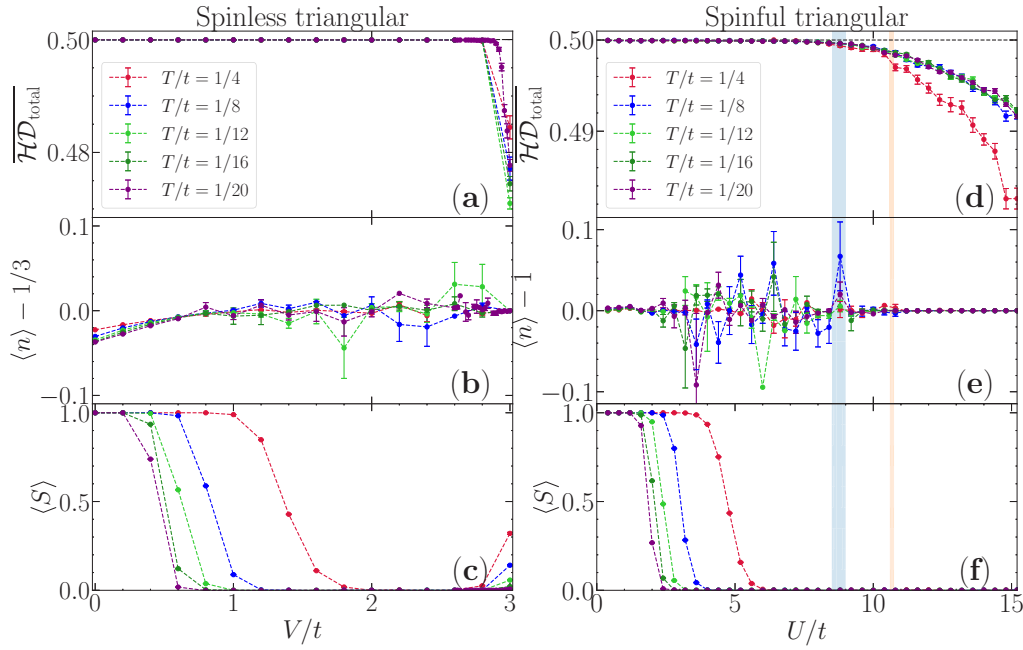
FIG. 13. Extra results for the triangular Hubbard model: The sign problem. (a)–(c) [(d)–(f)] From top to bottom, the average total Hamming distance, the averaged density subtracted by the target one, and the average sign of the weights in the Monte Carlo sampling for the U(1) [SU(2)] triangular Hubbard model. Results are shown for different temperatures as marked; in both cases, the results are for lattices with $L = 12$ and $t\Delta\tau = 0.1$. The vertical shaded regions in (d)–(f) have the same characteristics as in the main text, marking the best known locations of the two consecutive phase transitions.

A precise characterization of this phase can be obtained by the charge structure factor,

$$S_{\mathbf{k}}^c = \frac{1}{N_s} \sum_{l,m}^{N_s} e^{i\mathbf{k}\cdot(\mathbf{r}_l - \mathbf{r}_m)} \langle (\hat{n}_l - 1/3)(\hat{n}_m - 1/3) \rangle. \quad \text{(F2)}$$

For $\mathbf{k} = (2\pi/\sqrt{3}, 2\pi/3) \equiv K$, a three-sublattice pattern occupancy is favored, whereas $\mathbf{k} = (2\pi/\sqrt{3}, 0) \equiv M$ describes a stripe density pattern. Figure 11(d) shows the structure factor at these two points, where both grow with V, but the K channel always has larger amplitude [Figs. 11(d) and 11(e)]. We thus conclude that there is a tendency of three-sublattice charge occupation, but a system-size scaling may clarify how these result on a finite-order parameter when approaching the thermodynamic limit.

We now describe the results of the spinful triangular Hubbard model at half filling on a lattice with 18 sites (Fig. 12). This lattice is similar to the YC3 cluster investigated within DMRG schemes [33,34], albeit with longitudinal size $L_x = 6$. As for the U(1) case, there is also a change of the momentum sector associated to the ground state at a small cluster size, which leads to a first order phase transition at $U/t \simeq 1.9$. This is seen in Fig. 12(a), which gives the gap between the $\vec{q} = (0,0)$ and $\vec{q} = (0, 4\pi/3)$ momentum sector ground states, $\Delta \equiv |E_{(0,0)}^{\text{GS}} - E_{(0,4\pi/3)}^{\text{GS}}|$, initially at small interactions at $E_{(0,0)}^{\text{GS}} > E_{(0,4\pi/3)}^{\text{GS}}$, while $E_{(0,0)}^{\text{GS}} < E_{(0,4\pi/3)}^{\text{GS}}$ past $U/t \simeq 1.9$.

Nonetheless, at larger interactions a more smooth behavior is observed, where the fidelity susceptibility displays a clear peak at $U/t \simeq 7.6$ [Fig. 12(d)], which coincides with the positions at which the potential energy $\varepsilon = U \sum_i \langle \hat{n}_{i\uparrow} \hat{n}_{i\downarrow} \rangle$ has an inflection point [Fig. 12(c)]. We thus believe this marks

a regime where the metal-Mott insulating transition takes place. Recent estimations using width-4 cylinders [33,35] put this transition in the range $U_{c1}/t = 8.5$–9. The nature of the intermediate region, dubbed a nonmagnetic insulator, is under current debate, which has been converging towards a gapped chiral spin liquid phase. Yet, recent results using finite-temperature simulations [34] show stripy antiferromagnetic spin correlations to be particularly pronounced there. For that reason, we compute the spin structure factor,

$$S_{\mathbf{k}} = \frac{1}{N_s} \sum_{l,m}^{N_s} e^{i\mathbf{k}\cdot(\mathbf{r}_l - \mathbf{r}_m)} \langle \hat{s}_l^z \hat{s}_m^z \rangle, \quad \text{(F3)}$$

where $\hat{s}_l^z \equiv \hat{n}_{l\uparrow} - \hat{n}_{l\downarrow}$ [owing to the SU(2)-symmetric nature of the Hamiltonian, total spin structure can be obtained by multiplying the results by three]. The results point out that although the spin structure factor at different momenta are all enhanced by the interactions [Fig. 12(e)], at the M point, which corresponds to the stripy antiferromagnetic spin correlations, a larger magnitude until $U/t \simeq 10$ indicates that such spin pattern is favored [Fig. 12(f)]. For values $U/t \gtrsim 10$, the K-spin structure factor dominates and a 120° Néel spin ordered state likely takes place. Again, it remains to be seen how these results converge when a proper finite-size scaling is performed, which remains elusive with the limited system sizes amenable to exact calculations.

APPENDIX G: SIGN PROBLEM IN NONBIPARTITE GEOMETRIES

It has been recently demonstrated that the average sign of the weights extracted over the course of the importance

sampling in quantum Monte Carlo simulations of various fermionic models can be used to both qualitatively [5] and quantitatively [6] identify the loci of quantum critical points. Here, we show that this analysis does not in principle hold in the case of the Hubbard model in the triangular lattice, both on its U(1) or SU(2) formulations, at least using the "standard" Hubbard-Stratonovich transformation described in Appendix A.

Figure 13 displays the average total Hamming distance, the average density, and the average total sign of fermionic weights at decreasing temperatures. First, we observe that the presence of the sign problem makes the extraction of a physical observable, such as the electronic density, exhibit large statistical fluctuations. Yet these are within reasonable bounds from the target density after systematically adjusting the chemical potential μ. Second, we note that although the Hamming distance closely captures the onset of the ordered phases, the same cannot be said in respect to the onset of the sign problem, which starts at values of interactions much smaller than the ones associated to the quantum critical points. This is a contrast to the results of Refs. [5,6] that deserve further investigation, in particular an analysis that takes into account other types of Hubbard-Stratonovich transformations.

APPENDIX H: ALTERNATE HUBBARD-STRATONOVICH TRANSFORMATION

The transformations that cast the quartic terms in fermionic operators in bilinear forms are in general not unique [23]. In particular, for the spinful models we studied, the transformation highlighted in Appendix A explicitly breaks the SU(2) symmetry of the Hamiltonian and is only recovered over the course of the sampling. Here we address how a different transformation affects the analysis of the Hamming distance. We employ the transformation [27]

$$e^{-\Delta\tau U(\hat{n}_{i\uparrow}+\hat{n}_{i\downarrow}-1)^2/2}$$

$$= \sum_{s_{i,\tau}=\pm1,\pm2} \gamma(s_{i,\tau}) \prod_\sigma e^{i\sqrt{\Delta\tau U/2}\,\eta(s_{i,\tau})(\hat{n}_{i\sigma}-1/2)} + \mathcal{O}(\Delta\tau^4),$$

(H1)

which introduces a four-valued discrete field $s_{i,\tau} = \pm1, \pm2$, with the real constants,

$$\gamma(\pm1) = 1 + \sqrt{6}/3, \quad \eta(\pm1) = \pm\sqrt{2(3-\sqrt{6})},$$

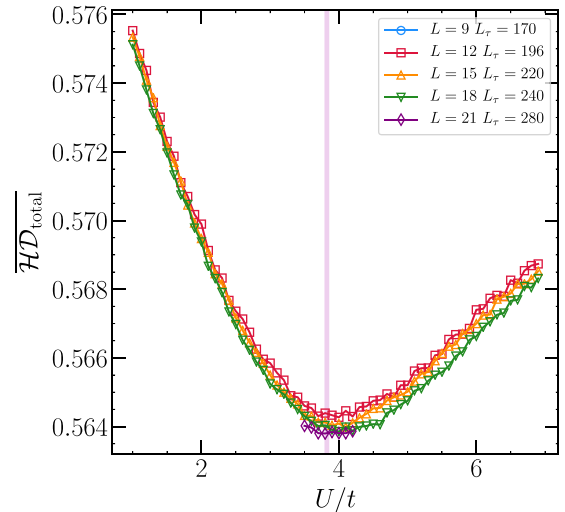$$\gamma(\pm2) = 1 - \sqrt{6}/3, \quad \eta(\pm2) = \pm\sqrt{2(3+\sqrt{6})}. \quad (H2)$$

FIG. 14. Average Hamming distance in the SU(2) honeycomb Hubbard model using the Hubbard-Stratonovich transformation of Eq. (H1). Here, $t\Delta\tau = 0.1$ and vertical shaded region depicts a confidence region of the QCP based on recent results [28–31]. The linear lattice sizes L and the number of imaginary-time slices L_τ are chosen such that $L_\tau/L^{0.5}$ is approximately constant [6].

In this case the transformation is not exact but the error introduced [$\propto\mathcal{O}(\Delta\tau^4)$] is negligible if compared to the one that arises from the Trotter decomposition [$\mathcal{O}(\Delta\tau^2)$]. Figure 14 shows the average Hamming distance of the SU(2) Hubbard model on the honeycomb lattice, computed as before, but now an expression like in Eq. (1) is generalized since the field is no longer binary. We notice again that a particular feature occurs in the vicinity of the critical point: A minimum at $\overline{\mathcal{HD}}_{\text{total}}$ with overall small finite-size effects. The values are seen substantially far from the uncorrelated value, 3/4, for this field with four components, and a reduced span of the phase space over the sampling is only observed close to U_c. These results highlight a deeper connection of the phases and the associate symmetry they break with the type of symmetry encoded on the Hubbard-Stratonovich transformation. Depending on the Hamiltonian investigated, types of decomposition that couple to other degrees of freedom, including fermionic pairs [60], might be beneficial in the analysis of the onset of other ordered regimes. Future investigation in further classes of models may clarify this.

[1] E. Y. Loh, J. E. Gubernatis, R. T. Scalettar, S. R. White, D. J. Scalapino, and R. L. Sugar, Sign problem in the numerical simulation of many-electron systems, Phys. Rev. B **41**, 9301 (1990).

[2] J. E. Hirsch, Two-dimensional Hubbard model: Numerical simulation study, Phys. Rev. B **31**, 4403 (1985).

[3] M. Troyer and U.-J. Wiese, Computational Complexity and Fundamental Limitations to Fermionic Quantum Monte Carlo Simulations, Phys. Rev. Lett. **94**, 170201 (2005).

[4] S. Wessel, B. Normand, F. Mila, and A. Honecker, Efficient quantum Monte Carlo simulations of highly frustrated magnets: The frustrated spin-1/2 ladder, SciPost Phys. **3**, 005 (2017).

[5] R. Mondaini, S. Tarat, and R. T. Scalettar, Quantum critical points and the sign problem, Science **375**, 418 (2022).

[6] R. Mondaini, S. Tarat, and R. T. Scalettar, Universality and critical exponents of the fermion sign problem, arXiv:2207.09026.

[7] Y. Mou, R. Mondaini, and R. T. Scalettar, The bilayer Hubbard model: Analysis based on the fermionic sign problem, Phys. Rev. B **106**, 125116 (2022).

[8] R. Blankenbecler, D. J. Scalapino, and R. L. Sugar, Monte Carlo calculations of coupled boson-fermion systems. I, Phys. Rev. D **24**, 2278 (1981).

[9] E. Loh and J. Gubernatis, Stable numerical simulations of models of interacting electrons in condensed-matter physics, in *Electronic Phase Transitions*, edited by W. Hanke and Y. Kopaev, Modern Problems in Condensed Matter Sciences Vol. 32 (Elsevier, Amsterdam, 1992), Chap. 4, pp. 177–235.

[10] R. Stratonovich, On a method of calculating quantum distribution functions, Sov. Phys. Dokl. **2**, 416 (1957).

[11] J. Hubbard, Calculation of Partition Functions, Phys. Rev. Lett. **3**, 77 (1959).

[12] J. E. Hirsch, Discrete Hubbard-Stratonovich transformation for fermion lattice models, Phys. Rev. B **28**, 4059 (1983).

[13] S. Sorella, The Hubbard-Stratonovich transformation and the Hubbard model, Int. J. Mod. Phys. B **05**, 937 (1991).

[14] P. Broecker, J. Carrasquilla, R. G. Melko, and S. Trebst, Machine learning quantum phases of matter beyond the fermion sign problem, Sci. Rep. **7**, 8823 (2017).

[15] K. Ch'ng, J. Carrasquilla, R. G. Melko, and E. Khatami, Machine Learning Phases of Strongly Correlated Fermions, Phys. Rev. X **7**, 031038 (2017).

[16] K. Ch'ng, N. Vazquez, and E. Khatami, Unsupervised machine learning account of magnetic transitions in the Hubbard model, Phys. Rev. E **97**, 013306 (2018).

[17] T. Mendes-Santos, X. Turkeshi, M. Dalmonte, and A. Rodriguez, Unsupervised Learning Universal Critical Behavior via the Intrinsic Dimension, Phys. Rev. X **11**, 011040 (2021).

[18] T. Mendes-Santos, A. Angelone, A. Rodriguez, R. Fazio, and M. Dalmonte, Intrinsic dimension of path integrals: Data-mining quantum criticality and emergent simplicity, PRX Quantum **2**, 030332 (2021).

[19] A. Tirelli and N. C. Costa, Learning quantum phase transitions through topological data analysis, Phys. Rev. B **104**, 235146 (2021).

[20] L. Wang, P. Corboz, and M. Troyer, Fermionic quantum critical point of spinless fermions on a honeycomb lattice, New J. Phys. **16**, 103008 (2014).

[21] Z.-X. Li, Y.-F. Jiang, and H. Yao, Solving the fermion sign problem in quantum Monte Carlo simulations by Majorana representation, Phys. Rev. B **91**, 241117(R) (2015).

[22] G. M. Buendia, Comparative study of the discrete and the continuous Hubbard-Stratonovich transformation for a one-dimensional spinless fermion model, Phys. Rev. B **33**, 3519 (1986).

[23] J. E. Hirsch, Connection between world-line and determinantal functional-integral formulations of the Hubbard model, Phys. Rev. B **34**, 3216 (1986).

[24] We note that the observation that $\alpha \to 1$ when $\Delta\tau U \to \infty$ is still compatible to the *single* approximation employed in the QMC, namely, the Trotter approximation, which gives rise to a controllable error $\propto U(\Delta\tau)^2$.

[25] R. T. Scalettar, R. M. Noack, and R. R. P. Singh, Ergodicity at large couplings with the determinant Monte Carlo algorithm, Phys. Rev. B **44**, 10502 (1991).

[26] T. Paiva, R. T. Scalettar, W. Zheng, R. R. P. Singh, and J. Oitmaa, Ground-state and finite-temperature signatures of quantum phase transitions in the half-filled Hubbard model on a honeycomb lattice, Phys. Rev. B **72**, 085123 (2005).

[27] Z. Meng, S. Wessel, A. Muramatsu, T. Lang, and F. Assaad, Quantum spin liquid emerging in two-dimensional correlated Dirac fermions, Nature (London) **464**, 847 (2010).

[28] S. Sorella, Y. Otsuka, and S. Yunoki, Absence of a spin liquid phase in the Hubbard model on the honeycomb lattice, Sci. Rep. **2**, 992 (2012).

[29] F. F. Assaad and I. F. Herbut, Pinning the Order: The Nature of Quantum Criticality in the Hubbard Model on Honeycomb Lattice, Phys. Rev. X **3**, 031010 (2013).

[30] F. Parisen Toldin, M. Hohenadler, F. F. Assaad, and I. F. Herbut, Fermionic quantum criticality in honeycomb and π-flux Hubbard models: Finite-size scaling of renormalization-group-invariant observables from quantum Monte Carlo, Phys. Rev. B **91**, 165108 (2015).

[31] Y. Otsuka, S. Yunoki, and S. Sorella, Universal Quantum Criticality in the Metal-Insulator Transition of Two-Dimensional Interacting Dirac Electrons, Phys. Rev. X **6**, 011029 (2016).

[32] T. Shirakawa, T. Tohyama, J. Kokalj, S. Sota, and S. Yunoki, Ground-state phase diagram of the triangular lattice Hubbard model by the density-matrix renormalization group method, Phys. Rev. B **96**, 205130 (2017).

[33] A. Szasz, J. Motruk, M. P. Zaletel, and J. E. Moore, Chiral Spin Liquid Phase of the Triangular Lattice Hubbard Model: A Density Matrix Renormalization Group Study, Phys. Rev. X **10**, 021042 (2020).

[34] A. Wietek, R. Rossi, F. Šimkovic, M. Klett, P. Hansmann, M. Ferrero, E. M. Stoudenmire, T. Schäfer, and A. Georges, Mott Insulating States with Competing Orders in the Triangular Lattice Hubbard Model, Phys. Rev. X **11**, 041013 (2021).

[35] B.-B. Chen, Z. Chen, S.-S. Gong, D. N. Sheng, W. Li, and A. Weichselbaum, Quantum spin liquid with emergent chiral order in the triangular-lattice Hubbard model, Phys. Rev. B **106**, 094420 (2022).

[36] C. Hotta and N. Furukawa, Strong coupling theory of the spinless charges on triangular lattices: Possible formation of a gapless charge-ordered liquid, Phys. Rev. B **74**, 193107 (2006).

[37] T. Koretsune, Y. Motome, and A. Furusaki, Exact diagonalization study of Mott transition in the Hubbard model on an anisotropic triangular lattice, J. Phys. Soc. Jpn. **76**, 074719 (2007).

[38] M. Miyazaki, C. Hotta, S. Miyahara, K. Matsuda, and N. Furukawa, Variational Monte Carlo study of a spinless fermion *tV* model on a triangular lattice: Formation of a pinball liquid, J. Phys. Soc. Jpn. **78**, 014707 (2009).

[39] P. Sahebsara and D. Sénéchal, Hubbard Model on the Triangular Lattice: Spiral Order and Spin Liquid, Phys. Rev. Lett. **100**, 136402 (2008).

[40] M. Laubach, R. Thomale, C. Platt, W. Hanke, and G. Li, Phase diagram of the Hubbard model on the anisotropic triangular lattice, Phys. Rev. B **91**, 245125 (2015).

[41] Changes in the layers selected or the unit cell across imaginary time employed do not lead to significant changes in the results.

[42] N. D. Mermin and H. Wagner, Absence of Ferromagnetism or Antiferromagnetism in One- or Two-Dimensional Isotropic Heisenberg Models, Phys. Rev. Lett. **17**, 1133 (1966).

[43] P. C. Hohenberg, Existence of long-range order in one and two dimensions, Phys. Rev. **158**, 383 (1967).

[44] S. Wessel and M. Troyer, Supersolid Hard-Core Bosons on the Triangular Lattice, Phys. Rev. Lett. **95**, 127205 (2005).

[45] T. Yoshioka, A. Koga, and N. Kawakami, Quantum Phase Transitions in the Hubbard Model on a Triangular Lattice, Phys. Rev. Lett. **103**, 036401 (2009).

[46] D. A. Huse and V. Elser, Simple Variational Wave Functions for Two-Dimensional Heisenberg Spin-$\frac{1}{2}$ Antiferromagnets, Phys. Rev. Lett. **60**, 2531 (1988).

[47] S. R. White and A. L. Chernyshev, Neél Order in Square and Triangular Lattice Heisenberg Models, Phys. Rev. Lett. **99**, 127004 (2007).

[48] K. Kanoda and R. Kato, Mott physics in organic conductors with triangular lattices, Annu. Rev. Condens. Matter Phys. **2**, 167 (2011).

[49] B. J. Powell and R. H. McKenzie, Quantum frustration in organic Mott insulators: From spin liquids to unconventional superconductors, Rep. Prog. Phys. **74**, 056501 (2011).

[50] Y. Shimizu, K. Miyagawa, K. Kanoda, M. Maesato, and G. Saito, Spin Liquid State in an Organic Mott Insulator with a Triangular Lattice, Phys. Rev. Lett. **91**, 107001 (2003).

[51] G. Li, A. E. Antipov, A. N. Rubtsov, S. Kirchner, and W. Hanke, Competing phases of the Hubbard model on a triangular lattice: Insights from the entropy, Phys. Rev. B **89**, 161118(R) (2014).

[52] T. Senthil, A. Vishwanath, L. Balents, S. Sachdev, and M. P. A. Fisher, Deconfined quantum critical points, Science **303**, 1490 (2004).

[53] Z.-X. Li, Y.-F. Jiang, S.-K. Jian, and H. Yao, Fermion-induced quantum critical points, Nat. Commun. **8**, 314 (2017).

[54] G. Parisi, Order Parameter for Spin-Glasses, Phys. Rev. Lett. **50**, 1946 (1983).

[55] H. G. Katzgraber and A. K. Hartmann, Ultrametricity and Clustering of States in Spin Glasses: A One-Dimensional View, Phys. Rev. Lett. **102**, 037207 (2009).

[56] M. Mezard, G. Parisi, and M. Virasoro, *Spin Glass Theory and Beyond* (World Scientific, Singapore, 1986).

[57] S. Hesselmann and S. Wessel, Thermal Ising transitions in the vicinity of two-dimensional quantum critical points, Phys. Rev. B **93**, 155157 (2016).

[58] L. Wang, Y.-H. Liu, and M. Troyer, Stochastic series expansion simulation of the $t-V$ model, Phys. Rev. B **93**, 155117 (2016).

[59] W.-L. You, Y.-W. Li, and S.-J. Gu, Fidelity, dynamic structure factor, and susceptibility in critical phenomena, Phys. Rev. E **76**, 022101 (2007).

[60] G. G. Batrouni and R. T. Scalettar, Anomalous decouplings and the fermion sign problem, Phys. Rev. B **42**, 2282 (1990).